IOPscience iopscience.iop.org

Home Search Collections Journals About Contact us My IOPscience

Characterization of an infrared detector for high frame rate thermography

This article has been downloaded from IOPscience. Please scroll down to see the full text article.

2013 Meas. Sci. Technol. 24 105403

(http://iopscience.iop.org/0957-0233/24/10/105403)

View the table of contents for this issue, or go to the journal homepage for more

Download details:
IP Address: 152.78.33.71
The article was downloaded on 01/09/2013 at 14:13

Please note that terms and conditions apply.

Meas. Sci. Technol. **24** (2013) 105403 (12pp) doi:10.1088/0957-0233/24/10/105403

Characterization of an infrared detector for high frame rate thermography

R K Fruehmann, D A Crump and J M Dulieu-Barton

Faculty of Engineering and the Environment, University of Southampton, University Road, Southampton, SO17 1BJ, UK

E-mail: janice@soton.ac.uk

Received 20 March 2013, in final form 5 July 2013
Published 30 August 2013
Online at stacks.iop.org/MST/24/105403

Abstract

The use of a commercially available photodetector based infrared thermography system, operating in the 2–5 μm range, for high frame rate imaging of temperature evolutions in solid materials is investigated. Infrared photodetectors provide a very fast and precise means of obtaining temperature evolutions over a wide range of science and engineering applications. A typical indium antimonide detector will have a thermal resolution of around 4 mK for room temperature measurements, with a noise threshold around 15 to 20 mK. However the precision of the measurement is dependent on the integration time (akin to exposure time in conventional photography). For temperature evolutions that occur at a moderate rate the integration time can be relatively long, enabling a large signal to noise ratio. A matter of increasing importance in engineering is the behaviour of materials at high strain rates, such as those experienced in impact, shock and ballistic loading. The rapid strain evolution in the material is usually accompanied by a temperature change. The temperature change will affect the material constitutive properties and hence it is important to capture both the temperature and the strain evolutions to provide a proper constitutive law for the material behaviour. The present paper concentrates on the capture of the temperature evolutions, which occur at such rates that rule out the use of contact sensors such as thermocouples and electrical resistance thermometers, as their response times are too slow. Furthermore it is desirable to have an indication of the temperature distribution over a test specimen, hence the full-field approach of IRT is investigated. The paper explores the many hitherto unaddressed challenges of IRT when employed at high speed. Firstly the images must be captured at high speeds, which means reduced integration times and hence a reduction in the signal to noise ratio. Furthermore, to achieve the high image capture rates the detector array must be windowed down, therefore there is a compromise made between the extent of the full-field imaging and the temporal resolution of the image capture. In the present work a maximum image capture speed of 15 kHz was achieved with a detector array of 64 $\times$ 12 elements and an integration time was 60 μs. Results from initial work on woven E-glass/epoxy tensile specimens are presented.

Keywords: infrared, thermography, calibration, high strain rate

(Some figures may appear in colour only in the online journal)

Introduction

The characterization of material behaviour when subjected to high strain rate loading is receiving increased attention by research groups around the world, as new enabling technologies are becoming available with which to conduct the tests [1]. This is motivated by a significant drive towards increased use of composite and sandwich materials for applications involving high speed blast and shock loading in both military and civilian sectors [2, 3]. To deploy these materials effectively in this area more must be known about their response at high strain rates.

 © 2013 IOP Publishing Ltd Printed in the UK & the USA

The vast majority of work in the area has focused on deriving precise strain measurements from high speed/high strain rate tests. An important consideration is that during a high strain rate event and failure, the material may heat considerably [4]. This is of particular relevance to the development of models where thermomechanical constitutive behaviour is important in assessing material performance and failure. Therefore to correctly implement the thermal aspects of the material response, accurate measures of temperature evolution are required. This is particularly necessary for polymeric materials, e.g., the Young's modulus of PVC foam decreases by as much as 10% for a modest temperature rise from 25 to 45 °C [5]. Therefore it is critical that thermal effects are accounted for in the development of constitutive laws describing the material behaviour.

A second important consideration relates to the spatial resolution of the measurement approach. The preferred experiment for investigating material response to high strain rate loading is the split Hopkinson pressure bar. This technique considers the global specimen response, and is as such unable to account for the local nature of failure initiation and propagation. Modern hydraulic test machines also exist that enable traditional test coupons to be tested at strain rates of the order of 10^2 strains per second. Traditional contacting sensors such as strain gauges, thermocouples, etc. are not ideal for use with compliant materials such as the polymer foams used in sandwich structures as they may locally stiffen and/or heat the material. Furthermore, they can provide information at only a single location on the specimen. The heterogeneous nature of more complex materials such as fibre reinforced polymer composites and foam cored sandwich structures therefore require a measurement approach able to capture local variations in the strain evolution. What is emerging in the literature and from industrial research partners is a clear need for full-field imaging of composite and foam specimens so that data from the whole specimen can be evaluated and localized failure regions identified.

The overall aim of the research described in this paper combines high speed white light and infrared imaging to provide both the strain evolutions (using digital image correlation (DIC)) and the temperature evolutions (using infrared thermography (IRT)) in a non-contact and high resolution manner. High speed white light imaging is relatively well established, although its use to quantitatively obtain strains using DIC is in its infancy. However, there are a number of papers in the literature, e.g. [6–8], that cite the use of high speed imaging for DIC. In the same way that strain measurement is moving from contact techniques (i.e. strain gauges) to non-contact imaging techniques (e.g. DIC), temperature measurement of high speed events is moving from thermocouples to IRT. The two main reasons cited in the literature echo those cited with respect to strain measurement, namely the invasive nature of thermocouples, and the limitation of being a single point measurement [9–11]. In addition, the requirement for thermal equilibrium between the thermocouple and the substrate, as well as strain rate dependent properties of the thermocouple itself introduce complications [12, 13]. However, the use of IRT is also not without challenges, in particular calibration, emissivity and background radiation sources are cited [14–17]. Truly high frame rate thermal imaging has been limited to only a few groups that have developed bespoke detector systems with up to 8 × 8 detector elements capable of frame rates up to 1 MHz [14, 18–20]. Other research has focused on the assessment of material properties and has relied on using commercial equipment to the limits of its capabilities, with frame rates of the order of a few 1000 Hz and detector arrays reduced to a small number of image pixels or even single lines, negating the full-field capabilities desired [9, 10, 17]. In many metallic specimens with relatively homogenous stress distributions and material composition, it can be argued that the full-field nature of the measurement is of secondary importance. However, for composite materials with a very heterogeneous composition, obtaining truly full-field temperature measurements is crucial. Going from single point measurements to imaging introduces new challenges regarding calibration of the detector. Therefore the object of the paper is to present a calibration approach applied to a commercial photodetector based IRT system at high image capture rates with a view to assessing the temperature evolution during high strain rate materials testing. Synchronizing white light (i.e. to obtain the strain evolutions from DIC) and infrared images has also been achieved and will be the subject of a further paper on the topic.

In the present paper the challenges associated with IR imaging at high speed are addressed in detail and it is clearly demonstrated that a commercial system can obtain quantitative values of temperature at rapid image capture rates. Improvements in detector technology have resulted in the possibility of using commercially available systems to acquire IR images at frame rates in the kHz region. This represents a sufficiently high acquisition rate to study a typical composite material's response at up to 10^2 strains per second. Two main factors have contributed to this: firstly, improvements in detector sensitivity to enable shorter exposure or integration times (IT), and secondly, the development of faster data processing electronics in the read-out circuits. However, the current technology is such that the detector is used well outside its normal operating parameters, and therefore a full detector characterization is required to obtain meaningful data. The paper describes, in detail, the characterization and calibration methodologies developed to enable quantitative data to be extracted at high frame rates.

Infrared thermography

IRT is a well documented field, with a variety of detectors being used in a wide range of applications [21]. Often however, IRT is applied in only a qualitative manner, because even with detectors calibrated by the manufacture the temperature measurement is dependent on the emissivity of the observed surface, which can vary across the scene. Quantitative techniques depend on a uniform emissivity often achieved by coating with a layer of matt black paint which even in a laboratory situation can introduce significant variations in response [22]. At high rates of temperature change, the time taken for heat to dissipate into the paint layer leads to a time lag,

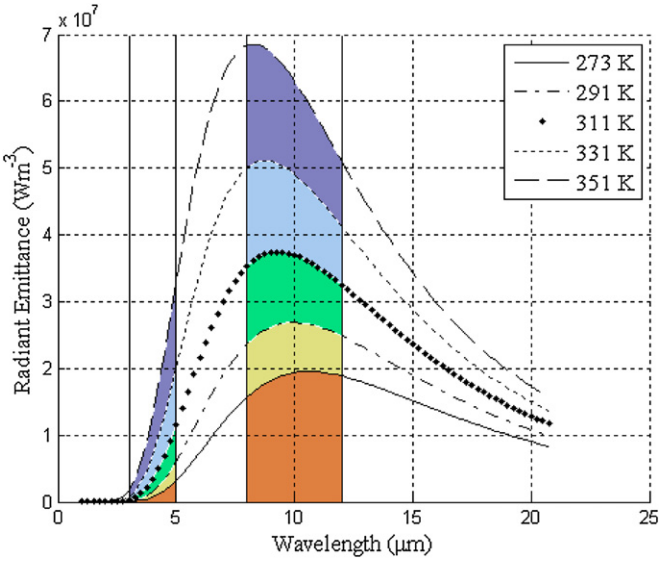

Figure 1. Isothermal curves of radiant emittance based on Planck's equation [1] with middle wavelength IR and long wavelength IR bands highlighted.

even though the paint layer is typically very thin, of the order of 10 to 15 microns [22]. A comprehensive background to IRT can be found in various text books such as [21]. Although familiar to many, to put the work into context, this section describes some of the basic physics of IRT, the nomenclature associated with IRT and the details of the particular IRT system used in the work described in the paper.

The radiation energy emitted at any given temperature can be calculated using Planck's law for any particular wavelength. This is commonly presented as isothermal lines showing the respective radiant emittance as a function of wavelength, as in figure 1. However, this applies to an idealized emission source known as a 'black body', defined as a source that absorbs equally and completely all incident radiation, regardless of the angle of incidence, spectral composition and polarization [21]. Real materials, however, will have a reduced emission, both in magnitude and wavelength spectrum, and therefore do not emit as black bodies; the remaining radiation is either transmitted or reflected. The emissivity is a function of surface preparation, with matt surfaces yielding a greater emissivity than smooth surfaces. Surface preparation for quantitative IRT therefore typically requires either the application of a high emissivity coating, or, light abrasion of the surface to produce a matt finish.

IR detectors can be classified into two groups: thermal detectors and photodetectors. Thermal detectors respond to incident radiation in the form of a temperature dependent electrical resistance change and typically have a broadband response but relatively slow response rate. Photodetectors by contrast tend to have a narrow band response and much higher response rates, responding directly to the incident radiation by means of a photoelectric effect. The response bandwidth defines the energy available for measurement at any given temperature. Two typical detector semiconductor materials (indium antimonide (InSb) and mercury cadmium telluride (MCT)) are sensitive either to the 3–5 μm or the 8–12 μm band [23], highlighted in figure 1. It is clear from figure 1 that the long wavelength IR band contains more energy at ambient temperatures, and therefore should provide the highest sensitivity in this temperature range. However, the 3–5 μm band provides a greater relative change in the radiated emittance with a change in temperature, and therefore is very well suited to techniques such as differential thermography or thermoelastic stress analysis [24]. The period over which the photons are collected is referred to as the integration time (IT) in the present work. There terminology is used because the measured response is proportional to the area under the curve in figure 1, integrated over the measurement interval, i.e. the IT.

The infrared detector system used in this work is a Cedip Silver 480M IR camera that represents the state-of-the-art photodetector from the year 2007. It comprises a 320 $\times$ 256 element InSb detector array, sensitive to the 3–5 μm wavelength band, with two read-out circuits per detector element to enable a *quasi*-continuous data capture. The detector is cryogenically cooled by means of a Stirling engine. The detector output is a 14 bit digital level (DL) bitmap with the analogue to digital conversion integral to the detector, i.e. 1 DL represents the smallest resolvable uncalibrated measurement increment with a full scale range of 2^{14} DL. A 27 mm lens provides a field of view from infinity to approximately 10 $\times$ 8 cm at maximum resolution. The IT is controlled by an electronic shutter and is adjusted by the user to suit the application and frame rate. The detector sensitivity is quoted as 4.2 mK/DL at 25 °C and an IT of 1300 μs, with an electronic noise of 17 mK (4.05 DL). The frame rate can be selected arbitrarily by the user, subject to an upper limit determined by 1/IT and the size of the image. When using the full detector array the maximum frame rate available is 383 Hz. By reducing the array size (referred to as sub-windowing) the achievable frame rate is increased, at the cost of either the field of view or spatial resolution. Similarly, a reduction in the IT increases the temporal resolution at the cost of thermal resolution as fewer photons impinge on the detector within the measurement period, thereby reducing the detector output signal. A compromise must therefore be made depending on the test parameters. Figure 2 shows a graphical representation of the compromise between frame rate, IT and array size; to increase the frame rate both the IT and the array size must be reduced. As the high strain rate events studied in this paper occur over very short time periods, the most critical parameter in the current work is frame rate. The minimum recording frequency is defined by the number of measurements required over the course of the test. Assuming the temperature evolution on the specimen surface is almost linear during the elastic portion of the test, two points would suffice to define the behaviour. At the end of the elastic deformation, a sudden change in temperature evolution is to be expected. As a design driver it was decided that a minimum of three temperature measurements were required during the test: one at the start, one at the mid-point and one at failure. In the current work, a hydraulic test machine (Instron VHS 80/20) capable of imparting strain rates of up to 10^2 strains per second is used. For a typical composite with a strain to failure of the order of 2%, this sets the minimum recording rate to 10 kHz.

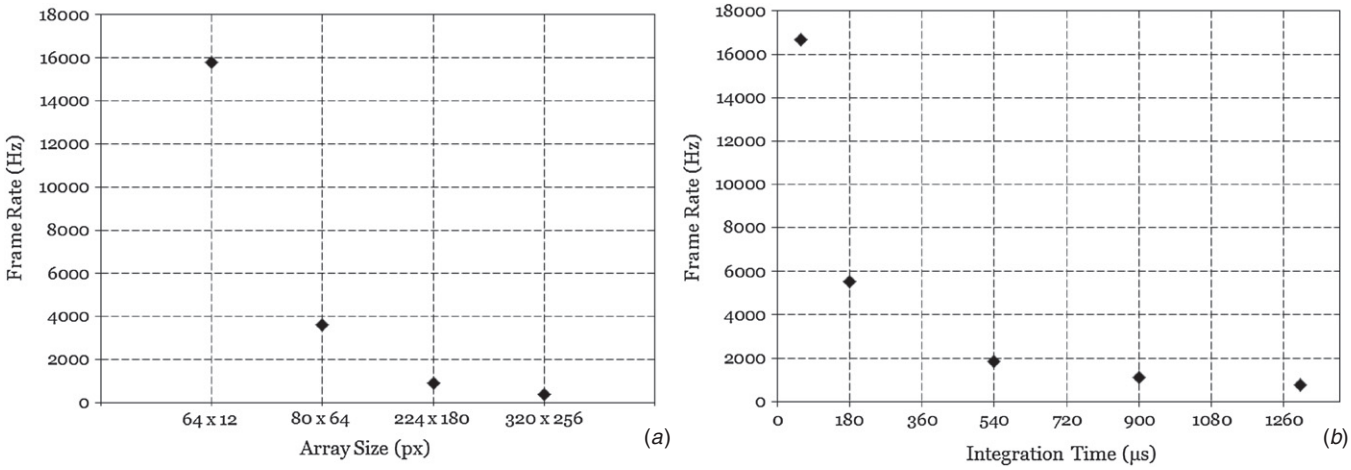

Figure 2. Relationship between (*a*) window size and frame rate and (*b*) integration time and frame rate.

A major motivation for this work has been to maintain a measurement array that could be termed 'full-field', so a minimum threshold can be set for the array size. The detector performance curves shown in figure 2 were used to select an IT of 60 μs and an array size of 64 $\times$ 12 pixels, leading to a maximum achievable frame rate of 15 840 Hz. The final detector characterization was conducted at 15 kHz to facilitate synchronization with white light cameras. This enabled the minimum recording rate of 10 kHz, as determined by the test duration, to be exceeded while maintaining a reasonable image size.

For any given detector, a calibration can be created that links the temperature of the observed body to the detector DL output. This is done by presenting the detector with a black body emitter at several discrete temperatures and then fitting a curve to the data. To carry out the calibration both the temperature and emissivity must be uniform across the entire black body. In a typical cavity black body, the emissivity is determined by the ratio of the aperture size to the cavity depth and internal surface area: the smaller the ratio, the higher the emissivity [25]. To illustrate this, a first order approximation of the emissivity for the case of a cylindrical cavity with a unit radius, depth D and aperture radius r taken from [26] is presented below:

$$\upsilon = 1 - \frac{ra^2}{D^2} \tag{1}$$

where υ is the emissivity and r is a measure of the dispersion of reflected radiation (akin to emissivity) of the internal surfaces of the cavity. It is clear that as the aperture is decreased relative to the depth of the cavity, the emissivity tends towards 1, irrespective of the nature of the internal surfaces of the cavity. Shape correction factors are required for more complex cavity geometries, a selection of which is provided in [25]. Hence, a smaller aperture enables a smaller cavity to be used which is easier to maintain at a uniform temperature, but can only be used over a small sub-set of the detector array. The calibration is therefore typically performed using the average DL value from a subset of elements from the total detector array. Thereby the precision and repeatability of the calibration is improved. Since each detector element (and the associated read-out circuit) has a slightly different response, a second step is required that relates the individual detector element response to that of the calibration subset. This second step is termed the non-uniformity correction (NUC) because it accounts for the variation across the detector array.

The variation in the sensitivity of each detector element has multiple sources including: (i) how they are mounted or doped, (ii) the manufacture of read-out circuit and (iii) analogue to digital converter. These are different for each element in the array, and importantly the operation of the read-out and the analogue to digital conversion changes with the size of the sub-window applied. The NUC process makes use of the linear relation between the detector digital output and the incident radiation. The standard procedure is to use a high emissivity plate at two different temperatures; the plate does not have to be a perfect black body but must emit uniformly across the entire field of view. Note also that the exact temperatures do not need to be known. The aim is to expose all detector elements to the same amount of radiation. The response of each element can then be plotted against the average DL value of the image subset used to obtain the calibration curve. Since the response of each element is linear, a straight line can be drawn between the two points from which a gain (gradient) and offset (y-intercept) can be calculated that relate the response of each individual detector element to that of the calibration subset for any measurement within the calibration range. This is shown schematically in figure 3, where the two dashed lines represent two detector elements with a different response compared with the average response of the calibration subset. Two correction factors (to adjust the gain and the offset) can then be obtained for each detector element, to align the detector element response with that of the calibration subset (solid line in figure 3). Once the NUC has been carried out the system is prepared to make quantitative temperature measurements. If any of the detector settings are changed, e.g. frame rate or array size, then the NUC must be carried out again as all these factors affect the detector response.

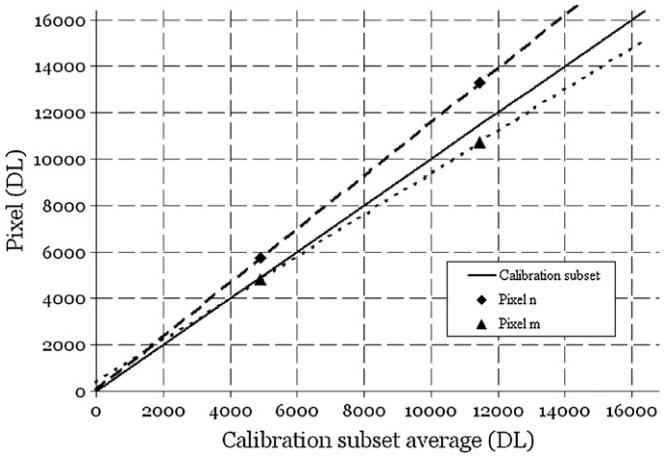

Figure 3. Linear fit for NUC.

High speed thermography

For the high speed thermography it was decided to target a frame rate of 15 kHz. Accordingly an IT of 60 μs and a sub-window size of 64 $\times$ 12 pixels were set (see figure 2). Although higher frame rates might be desirable for high strain rate testing, this was considered to be a reasonable compromise with the currently available technology. The use of the short IT for temperature measurements at ambient temperatures means that the signal available for measurement is very small, generating a detector response of the order of 500 DL around 20 °C and 1000 DL at 60 °C. This represents 3% to 6% of the total detector range. The manufacturer does not recommend extrapolating the standard calibration curves beyond 30% at the lower end because at such very low levels of signal the detector response changes. This is because with the small number of photons impinging on the detector it cannot be assumed that the detector is behaving in a linear fashion. Therefore, a bespoke calibration is required for high speed thermography.

The first step in characterizing the detector for high frame rates was to apply the two-step approach described above, obtaining a calibration curve on a detector sub-set and then applying a NUC. A calibration was conducted over a temperature range from 4 to 75 °C with a cavity black body using water circulation for temperature regulation. The black body has a bi-conical cavity with an aperture diameter of 30 mm and a cavity depth of 90 mm, with an estimated emissivity greater than 0.997. A series of videos (20 images each) was collected at discrete temperature increments (every 2 K). The NUC was conducted at 10 and 30 °C. The quality of the calibration was evaluated firstly by calculating the noise in each detector element, calculated as the standard deviation from ten readings, giving two values for each detector element to correspond with the two read-out circuits. This was shown to be between 1.5 and 2.5 DL for most detector elements, with a few detector elements having a standard deviation up to a maximum of 3.5 DL at 50 °C. Secondly, the standard deviation was calculated over the image. Here a sudden increase in the standard deviation was noted around 45 °C. To investigate this further, the image histogram was plotted at 20, 30, 40, 50 and 60 °C (see figure 4). This shows a symmetrical distribution about a single maximum at temperatures up to 40 °C. However, at 50 °C, the distribution across the image begins to show two distinct peaks and a greatly increased spread. Close inspection of the image reveals a striation pattern forming at the higher temperatures as shown in figure 5(*a*)). The striation pattern can be directly linked to the detector construction, as can be seen in figure 5(*b*)) which shows a full-frame image without the NUC applied. This indicates that there is a deviation in the actual response of the detector elements from linear behaviour assumed in the NUC procedure, clearly demonstrating a shortcoming in the standard NUC procedure, making it unsuited to calibrations for high speed IRT where small ITs are used at room temperature.

To account for the detector nonlinear response a possible solution might be to conduct the NUC at multiple temperatures and fitting a higher order function, rather than a line. This may require many points to achieve a good fit, in addition to the calibration data-set obtained for the particular IT. Furthermore the NUC would be a function of a high order polynomial rather than a simple linear fit, which adds complexity and introduces potential for further errors. Therefore an alternative approach was adopted where a calibration curve was obtained for each detector element individually, thereby taking into account the image non-uniformity and detector nonlinearity in a single step. For this it is necessary to have a black body with a

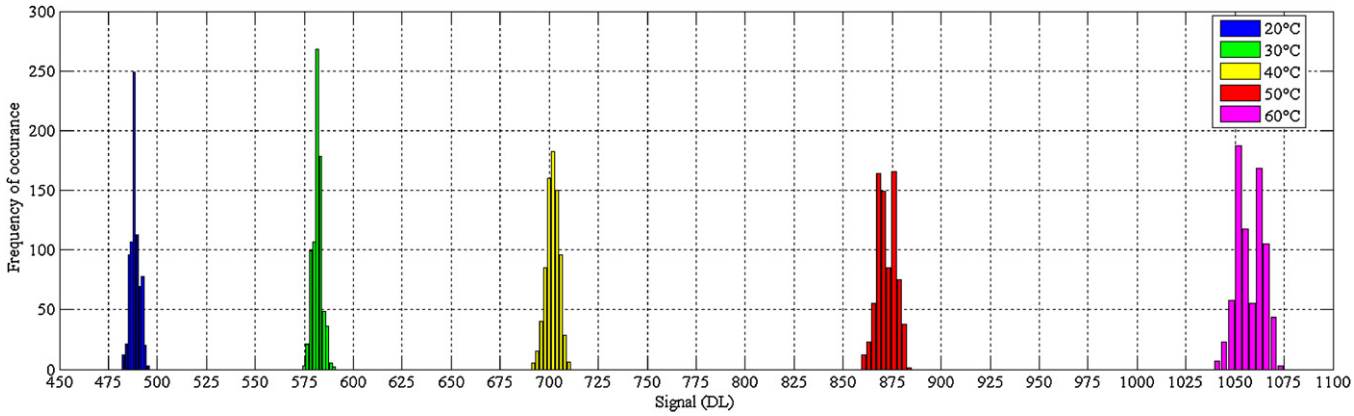

Figure 4. Histogram of image noise at different temperatures.

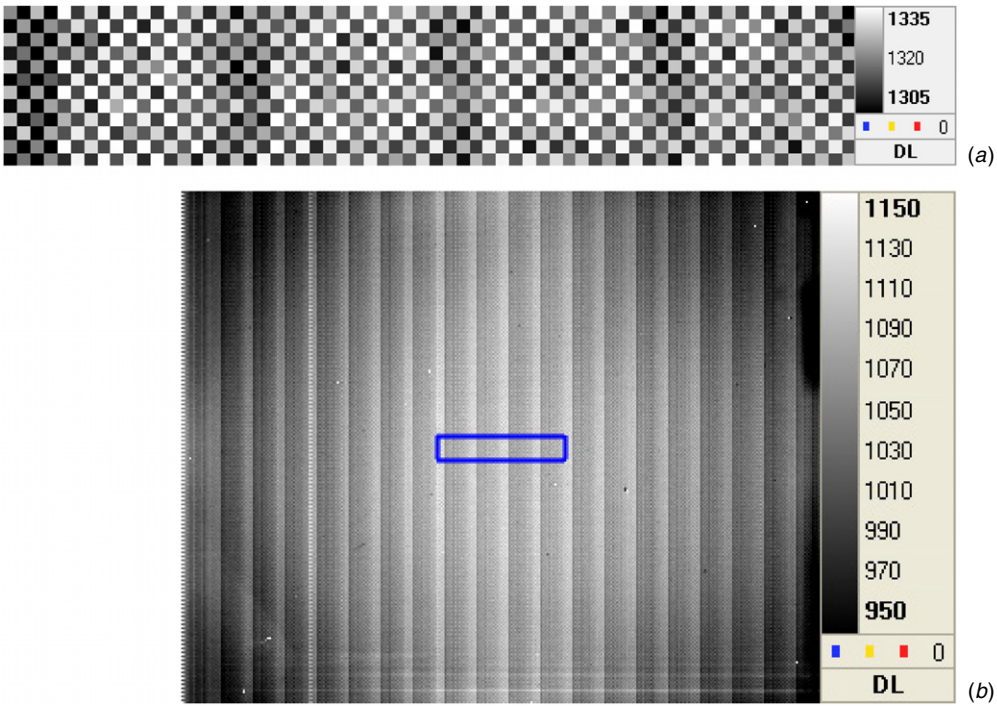

Figure 5. (*a*) 64 × 12 sub-windowed image of black body at 344 K with NUC applied, (*b*) full frame (320 × 256) image without NUC of ambient temperature uniform emission target showing the location of the 64 × 12 pixel sub-window.

sufficiently large area to cover the entire (sub-windowed) field of view. Due to the detector design having two sets of read-out circuits, two calibration curves are required for each image pixel, however, the full set of calibration curves can be obtained in a single set of measurements.

The calibration data have been interpolated using a spline fit in MatLab. A sample of the calibration curves is shown in figure 6, illustrating both the significant differences between odd and even frames, as well as the differences between individual detector elements in the array, hence justifying the need for the detector element by element calibration.

Calibration/assessment of measurement precision

To assess the accuracy of a measurement is very difficult as this assumes knowledge of a 'true' value. While the black body has a calibrated thermocouple, this is a point measurement that is unable to account for variations of temperature within the cavity, although these are assumed to be very small. However, it is possible to assess the precision, or uncertainty interval of the measurement, and this will be the focus in assessing the performance of the system. Each point on the calibration curve is obtained as the average of 20 images (a 40 image video was obtained every 2 K and the odd and even frames separated). The first investigation of measurement precision took the form of plotting the standard deviation of each calibration point and plotting this as a histogram for the full image. This is shown for selected temperatures across the calibration range in figure 7. It can be seen that the standard deviation (in terms of DL) does not vary greatly with temperature; there is a slight shift of the histogram peak at the higher temperatures of approximately 0.5 DL to the right, with over 80% of all detector elements having a standard deviation of 2.5 DL or less. The distribution of this uncertainty across the image was also investigated. Figure 8 shows the pixel standard deviations across the entire field of view at six different temperatures. From this it can be seen that there is no pattern across the image, and that no individual image pixels have a consistently better or worse performance. The 2 to 2.5 DL uncertainty in the detector calibration is consistent across the full temperature range and all image pixels, for both odd and even frames.

The second step was to investigate if the noise pattern from the black body changes when imaging a 'real' surface. For this purpose an E-glass/epoxy specimen prepared with a matt finish was used. The ambient temperature was 23.8 °C, measured using a K-type thermocouple. Since the specimen did not cover the full-field of view, only the central portion of the image has been analysed, as shown in figures 9 and 10. The distribution of pixel standard deviations across the field of view (figure 9) and the corresponding image histogram of pixel standard deviations (figure 10) show the same characteristics as the calibration images in both distribution and magnitude.

The detector sensitivity and the measurement confidence interval (precision) were thereby determined over the full temperature range of the calibration. This is summarized in table 1 which presents the aggregate detector sensitivity (temperature increment per DL) and precision (detector pixel standard deviations calibrated into °C) over the measurement range.

The final step in the calibration procedure is to account for emissivity and background radiation sources. For a surface with an emissivity less than 1, the radiation emanating from the surface will comprise a portion that is emitted and a portion that is a reflection of the background radiation. If the background

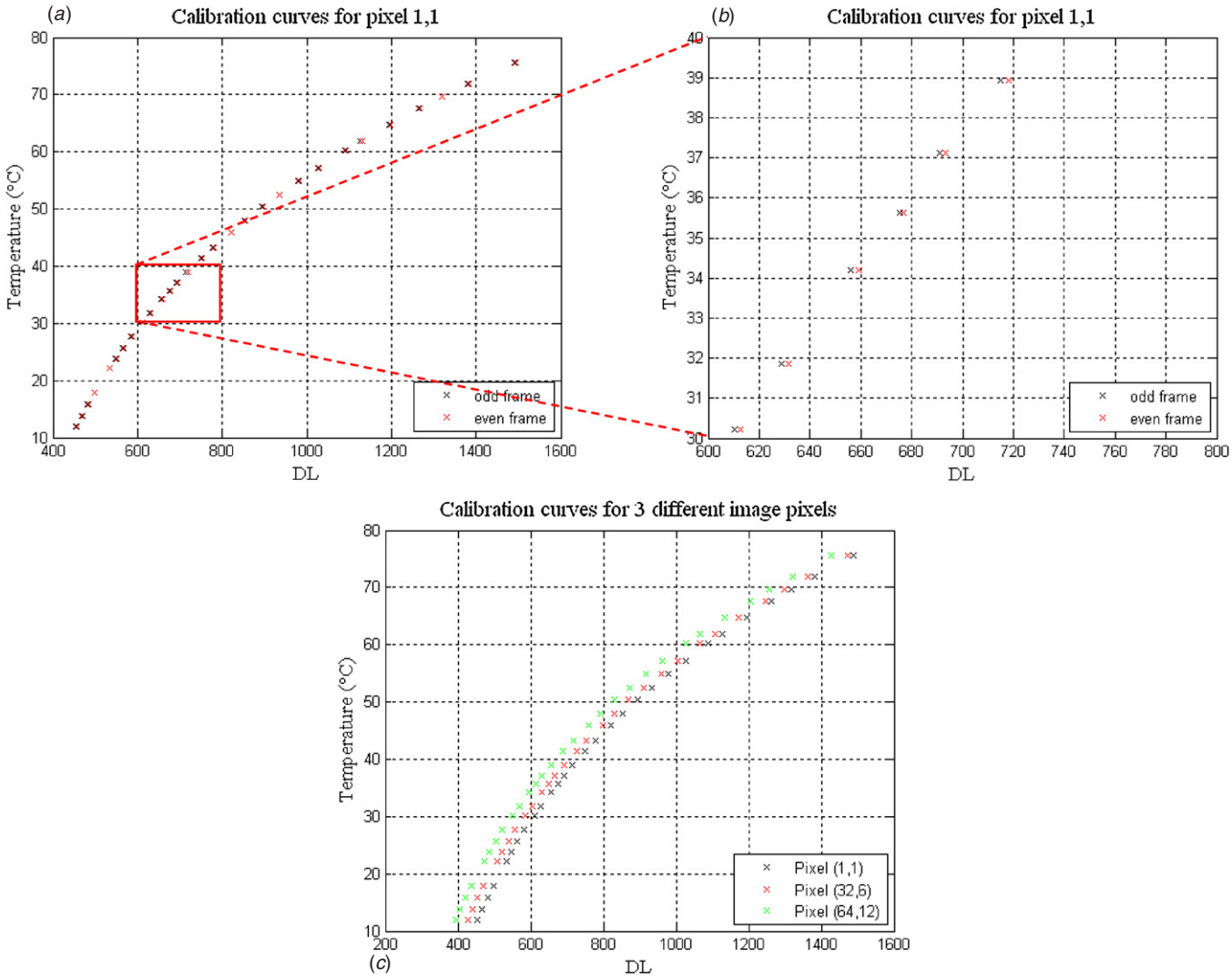

Figure 6. Calibration curves for selected image pixels, (*a*) pixel (1,1) odd and even, (*b*) pixel (1,1) enlarged—odd and even and (*c*) three different pixels (1,1), (32,6) and (64,12).

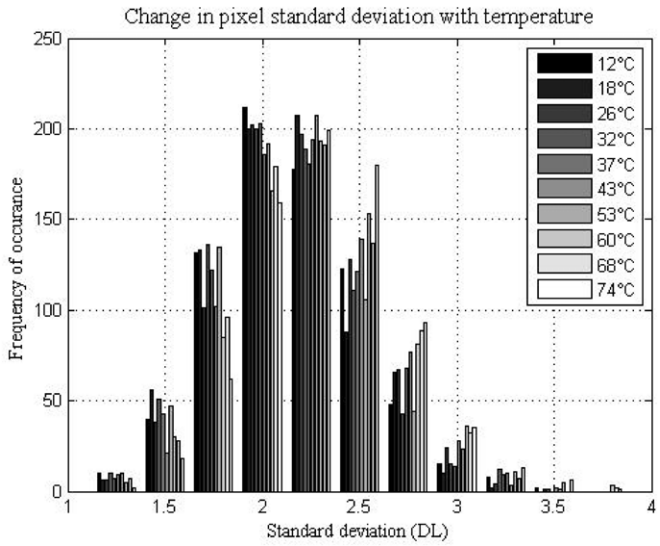

Figure 7. Image histogram of pixel standard deviation (over 20 frames) at different temperatures across the calibration range.

Table 1. Detector precision.

Temperature (°C)	Sensitivity (°C/DL)	Precision (°C)
15	0.14	0.32
25	0.11	0.24
35	0.08	0.19
45	0.06	0.14
55	0.05	0.11
65	0.04	0.09
75	0.03	0.07

temperature is roughly uniform, i.e. there are no particularly hot or cold objects, then the background can be assumed to emit as a black body of the same temperature. The radiation reaching the detector can then be written as

$$\Phi_{\text{tot}} = \upsilon\Phi_{\text{BBs}} + (1 - \upsilon)\Phi_{\text{BBb}} \tag{2}$$

where υ is the emissivity, Φ_{tot} is the total photon flux emanating from the surface, Φ_{BBs} is the photon flux emitted from a black body at the equivalent temperature to the surface, and Φ_{BBb} is the photon flux emitted by a black body at the

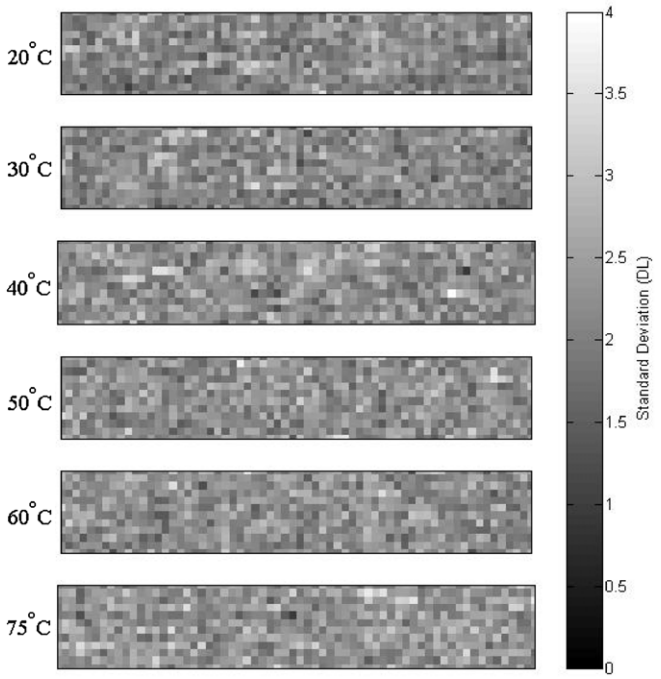

Figure 8. Images of pixel standard deviations at different temperatures.

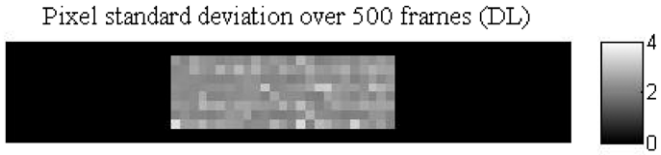

Figure 9. Pixel standard deviation over 500 frames from real surface (E-glass/epoxy).

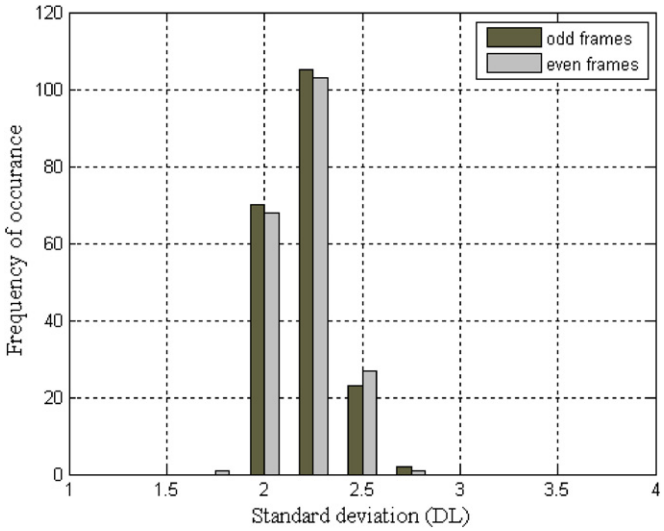

Figure 10. Histogram of pixel standard deviation over 500 frames from real surface (E-glass/epoxy).

equivalent temperature to the background. It is necessary to extract Φ_{BBs} from the total recorded photon flux in order to perform the calibration. Since the detector responds directly to the incoming photon flux (Φ_{tot}) it is necessary to know the emissivity of the surface and the temperature of the background to obtain accurate temperature measurements from the specimen surface. In a typical experimental setup, the specimen will initially be at equilibrium with the environment, and therefore Φ_{BBs} and Φ_{BBb} will be equal at the start. A uniform background radiation field can be achieved by draping a curtain around the test area as a shield.

Test results

Two E-glass/epoxy tensile specimens with four plies of 200 g m^{-2} plain woven roving (RE210D manufactured by Gurit) were tested at two different strain rates. The warp yarns were aligned parallel to the loading direction. The specimens were 25 mm wide, 150 mm long with 50 mm end tabs and a 12 mm wide gauge area with 6 mm radii cut either side, as shown in figure 11. The geometry was selected to ensure that failure occurred within the field of view of the detector, approximately 5 $\times$ 27 mm^2. With warp and weft yarn spacings of 1.1 mm and 1.7 mm respectively, this gives approximately 2 $\times$ 6 weave cells within the field of view. (At the narrowest point there were still at least 6 unit cells of the weave pattern across the specimen width.) The mechanical load was applied using an Instron VHS 80/20 hydraulic test machine at actuator velocities of 5 and 10 m s^{-1}, corresponding to strain rates of approximately 50 and 100 s^{-1}. The IR detector was triggered to record from 30 ms before the start of the loading. The load to failure was recorded using a piezoelectric Kistler load cell. The two specimens failed at a peak stress of 365 MPa in the narrowest gauge section. The key results are presented in figures 12–15.

The calibrated IR images from the 5 m s^{-1} test are shown in figure 12. The specimen outline has been approximately overlaid on the first image for orientation. The first image was obtained just before the load was applied, and only every other image up to failure is shown. A monotonic decrease in the specimen temperature can be observed in the first four images, corresponding to the thermoelastic effect [27]. Figure 13 shows the temperature evolution of a 2 $\times$ 2 pixel area. (The area is highlighted by a black square in all five images in figure 12.) The thermoelastic temperature change is 1 K $\pm$ 0.24 K between initial load and just before failure, as highlighted by the insert in figure 13. Taking literature values of density (1980 kg m^{-3}), coefficient of thermal expansion (17 $\times$ 10^{-6} K^{-1}, average of parallel and transverse to fibres) and heat capacity (828 J kg^{-1} K^{-1}) [28] gives an estimated thermoelastic temperature change of 1.1 K. Although only a rough estimate, this close correlation demonstrates the ability to measure small temperature changes with a high degree of confidence. In the fourth image in figure 12 two 'hot spots' can be seen at either specimen edge. These are interpreted as failure initiation points. The fifth image shows the edge of the fractured specimen, the lower half has disappeared from the field of view. (Note that the temperature scale has been adjusted for the final image after failure to enable the much greater temperature range across the specimen surface to be visualized.) The two areas identified as failure initiation points are no longer the hottest part of the specimen. This could

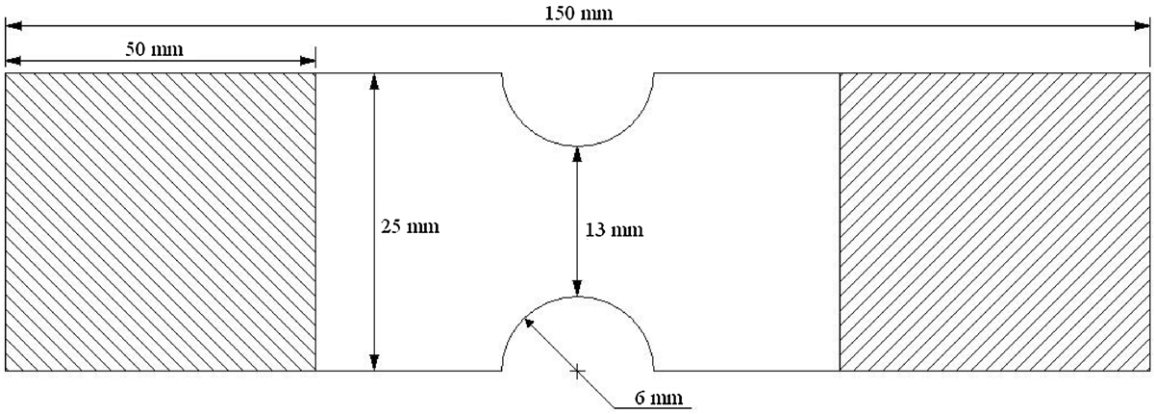

Figure 11. Schematic of nominal specimen geometry between the grips.

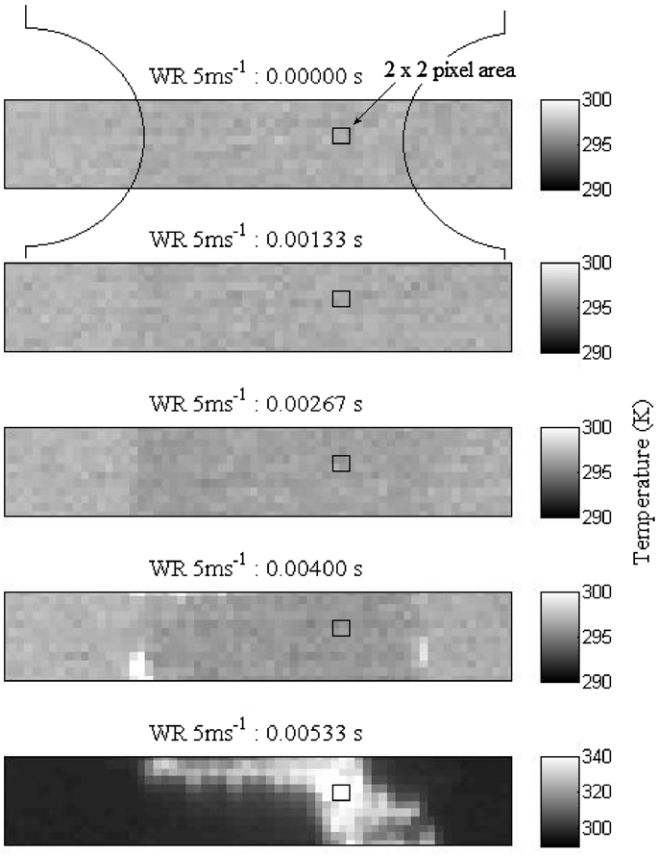

Figure 12. Calibrated IR images from one frame before the application of load, to failure at 5 m s^{-1} actuator speed, with an approximate outline to the specimen overlaid on the first image.

be attributed to multiple effects, for example, on failure the material may have parted from the rest of the specimen and left the field of view.

Analysing the portion of the plot in figure 13 beyond failure of the specimen enables the heat released due to the fracture to be estimated. Taking the above book value for the heat capacity, the temperature change of roughly 60 K corresponds to a heat release of approximately 50 kJ kg^{-1}. Averaging this value across the 2 × 2 pixel volume gives an energy release of 160 J for a volume of 1.7 mm^3. The temperature increase at failure must be related to the energy released as the material fails and therefore it is postulated that it may be possible to identify different types of failure based on the temperature evolutions. A post mortem inspection showed the damage in the 2 × 2 pixel area shown in figure 13 to include significant delamination between the woven rovings. By contrast, the fracture edge towards the middle of the specimen had a much less ragged edge, indicating that the failure was primarily fibre breakage. The temperature change at fracture from this region was approximately 30 K, i.e. half of that in the delaminated region. The energy released is more difficult to quantify accurately since the heat generated by the fibre breakage is concentrated within a much smaller area and the measurement is therefore averaged over a portion of the adjacent material, which would lead to a reduction in the calculated energy release per unit volume. The difference in failure mechanism in the central portion of the specimen compared to the specimen edges is not surprising, since through thickness stresses arise at the edge of a laminate that promote delamination, especially when combined with damage that might have been caused in the cutting process, neither of which exist in the centre of the specimen. The example illustrates the additional information that can be captured in a single test through the use of full-field thermography that is important in such heterogeneous materials as composites.

At the higher strain rate, less data is available for capture, allowing only four images to be captured from the first application of load through to failure, shown in figure 14. Again the specimen outline has been overlaid on the first image prior to the application of load for orientation. An initial decrease in temperature (approximately 0.8 K) can also be observed in the first three images. The measured change in temperature is slightly less due to integration across a rapidly changing field. In the third image, two failure initiation points are clearly visible at the bottom left and top right of the specimen. The plots in figure 15 show the temperature of three different 2 × 2 pixel areas, one on the lower left initial failure location (black crosses), one on the top right initial failure location (blue triangles) and one from just to the left of the centre of the specimen (red circles) where the greatest

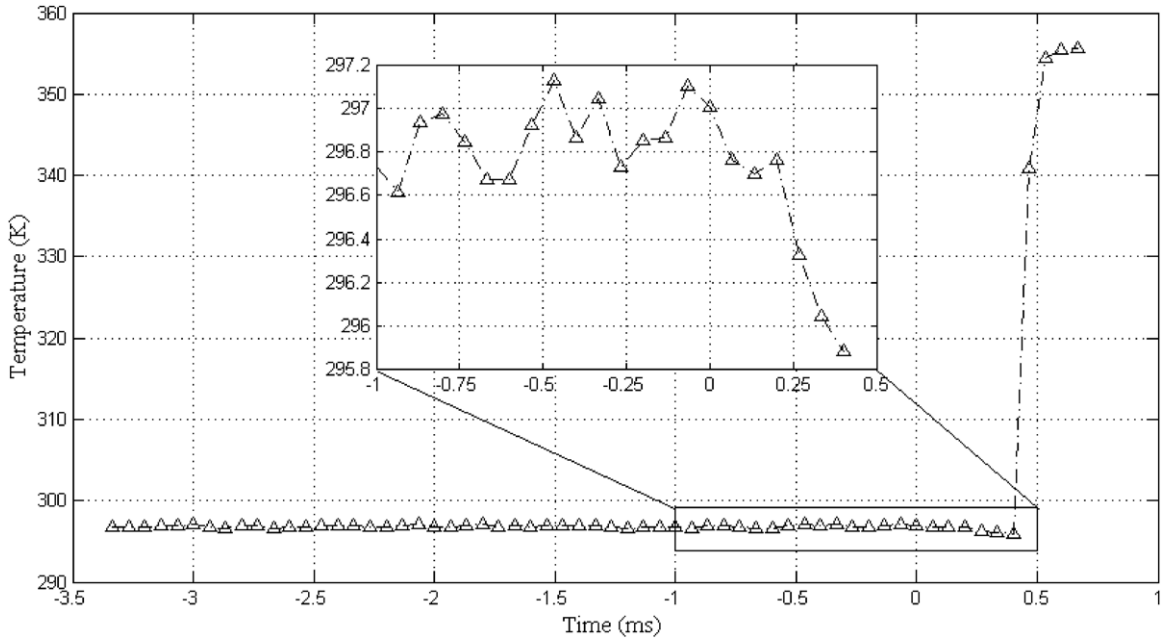

Figure 13. Temperature evolution over a 2 × 2 pixel area at 5 m s^{-1} actuator speed—zoomed insert highlights temperature evolution during the elastic portion of the test.

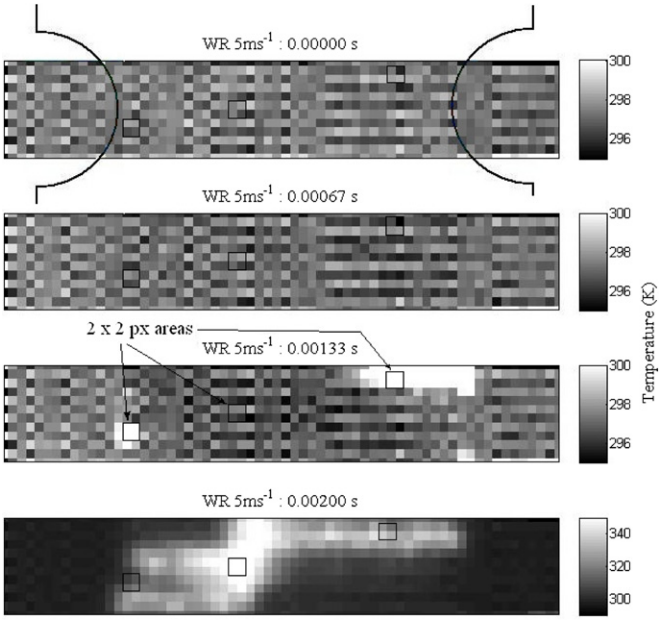

Figure 14. Calibrated IR images from one frame before the application of load, to failure at 10 m s^{-1} actuator speed, with an approximate outline to the specimen overlaid on the first image.

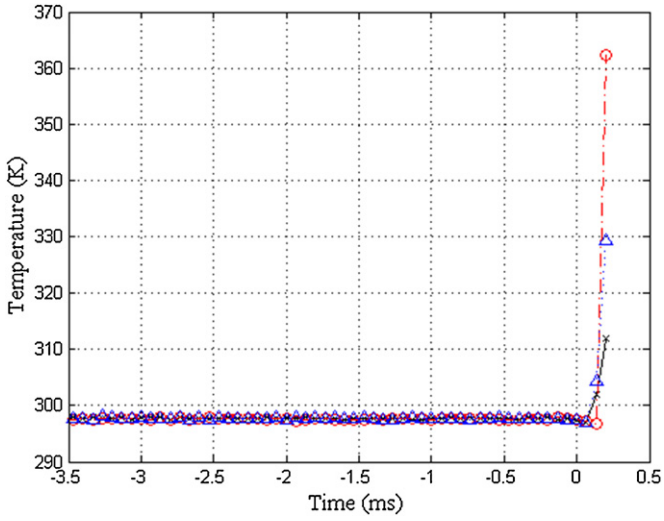

Figure 15. Temperature evolution over three 2 × 2 pixel areas at 10 m s^{-1} actuator speed—black crosses: bottom left failure initiation point, red circles: area of greatest heating and blue triangles: top right failure initiation point.

heating took place. Again, a post mortem inspection identified the same two failure mechanisms as at the lower strain rate, and the corresponding temperature changes of 60 K for the delamination and 30 K for the fibre break regions apply. The temperature change at the lower left failure initiation point was, however, significantly smaller and this could be due to a significant portion of material remaining connected to the lower half of the specimen which disappeared from the field of view.

Conclusions

The importance of understanding how the behaviour of an IR detector changes at the limits of its sensitivity has been demonstrated. Apparently straightforward processes such as the NUC may not perform as expected when operating outside the detector's normal range. A methodology has therefore been developed that enables a general calibration to be obtained for any IR array detector, outside its region of linear response. This involves obtaining a calibration for each

detector element individually. This methodology thereby also enables the measurement uncertainty to be easily quantified for each image pixel independently. While the current study has been conducted with a six-year-old detector, a review of other detectors currently on the market suggests that the primary change with regards to acquisition speed has been in the development on new read-out circuits. While this brings with it the possibility of obtaining larger images at high frame rates, it is not accompanied with a corresponding increase in sensitivity. Sensor technology developments have been driven by increase in frame size rather than frame rates. Hence, the challenge of temperature calibration for ambient temperature, high speed measurements currently remains as described.

The calibration has then been applied to temperature measurements from a composite specimen subjected to a high strain rate tensile load. The thermal sensitivity was sufficiently precise to identify the small temperature change associated with the thermoelastic effect, and the measured value corresponds well with a simple calculation. This provides confidence in the fidelity of temperature change measurements obtained using the described calibration procedure. An estimate of the energy release associated with failure has also been calculated and a correlation to different failure modes, as identified in a post mortem inspection, was demonstrated. This detailed information can only be obtained as a result of calibrated full-field temperature measurements. Although further investigation into the correlation between heat release and failure mode is beyond the scope of the current work, the calibration process above provides a suitably reliable temperature measurement to enable such work to be conducted in future. The ability to reliably measure temperature at high acquisition rates forms a significant milestone in obtaining a complete characterization of composite materials at high strain rates.

Acknowledgments

The research was funded by the Engineering and Physical Sciences Research Council (EPSRC) and the Defence and Science Technology Laboratories (DSTL). We would like to thank the continuing support of the numerous academic and industrial collaborators who formed the industrial advisory board during the project as follows; Aalborg University, Airbus, Arts et Métiers ParisTech, FLIR ATS, GE Aviation, LaVision, Lloyd's Register.

References

[1] Hamouda A M S and Hashmi M S J 1998 Testing of composite materials at high rates of strain: advances and challenges *J. Mater. Process. Technol.* **77** 327–36

[2] Daniel I M, Werner B T and Fenner J S 2011 Strain-rate-dependent failure criteria for composites *Compos. Sci. Technol.* **71** 357–64

[3] Gilat A, Goldberg R K and Roberts G D 2002 Experimental study of strain-rate-dependent behaviour of carbon/epoxy composite *Compos. Sci. Technol.* **62** 1469–76

[4] Noble J P, Goldthorpe B D, Church P and Harding J 1999 The use of the Hopkinson bar to validate constitutive relations at high rates of strain *J. Mech. Phys. Solids* **47** 1187–206

[5] Zhang S, Dulieu-Barton J M, Fruehmann R K and Thomsen O T 2011 A methodology for obtaining material properties of polymeric foam at elevated temperatures *Exp. Mech.* **52** 3–15

[6] Godara A and Raabe D 2007 Influence of fiber orientation on global mechanical behavior and mesoscale strain localization in a short glass-fiber-reinforced epoxy polymer composite during tensile deformation investigated using digital image correlation *Compos. Sci. Technol.* **67** 2417–27

[7] Tiwari V, Sutton M and McNeil S 2007 Assessment of high speed imaging systems for 2D and 3D deformation measurements: methodology development and validation *Exp. Mech.* **47** 561–79

[8] Koerber H, Xavier J and Camanho P P 2010 High strain rate characterization of unidirectional carbon-epoxy IM7–8552 in transverse compression and in-plane shear using digital image correlation *Mech. Mater.* **42** 1004–19

[9] Walley S M, Proud W G, Rae P J and Field J E 2000 Comparison of two methods of measuring the rapid temperature rises in split Hopkinson bar specimens *Rev. Sci. Instrum.* **71** 1766–71

[10] Nowacki W K, Gadaj S P and Pieczyska E A 2002 Measurement of temperature during simple dynamic shear *Proc. 6th Conf. on Quantitative Infrared Thermography* pp 185–91

[11] Regev A and Rittel D 2008 Simultaneous transient temperature sensing of impacted polymers using infrared detectors and thermocouples *Exp. Mech.* **48** 675–82

[12] Bloomquist D D and Sheffield S A 1980 Thermocouple temperature measurements in shock-compressed solids *J. Appl. Phys.* **51** 5260–6

[13] Rabin Y and Rittel D 1999 A model for the time response of solid-embedded thermocouples *Exp. Mech.* **39** 132–6

[14] Trojanowski A, MacDougall D and Harding J 1998 An improved technique for the experimental measurement of specimen surface temperature during Hopkinson-bar tests *Meas. Sci. Technol.* **9** 12–19

[15] Gadaj S P, Nowacki W K and Pieczyska E A 2002 Temperature evolution in deformed shape memory alloy *Infrared Phys. Technol.* **43** 151–5

[16] Guzmán R, Meléndez J, Aranda J M, Essa Y E, López F and Pérez-Castellanos J L 2009 Measurement of temperature increment in compressive quasi-static and dynamic tests using infrared thermography *Strain* **45** 179–89

[17] Pérez-Castellanos J-L and Rusinek A 2012 Temperature increase associated with plastic deformation under dynamic compression: application to aluminium alloy AL 6082 *J. Theor. Appl. Mech.* **50** 377–98

[18] Zehnder A T, Guduru P R, Rosakis A J and Ravichandaran G 2000 Million frames per second infrared imaging system *Rev. Sci. Instrum.* **71** 3762–8

[19] Zehnder A T, Rosakis A J and Ravichandaran G 2001 High speed infrared imaging system *US Patent Specification* US006268883B1

[20] Guduru P R, Rosakis A J and Ravichandaran G 2001 Dynamic shear bands: and investigation using high speed optical and infrared diagnostics *Mech. Mater.* **33** 371–402

[21] Bramson M A 1968 *Infrared Radiation: A Handbook for Applications* (New York: Plenum)

[22] Robinson A F, Dulieu-Barton J M, Quinn S and Burguete R L 2010 Paint coating characterization for thermoelastic

stress analysis of metallic materials *Meas. Sci. Technol.* **21** 085502
[23] Norton P 2002 HgCdTe infrared detectors *Opto-Electron. Rev.* **10** 159–74
[24] Dulieu-Barton J M 2011 Measurement of thermomechanical coupling and its application in stress and damage analysis *Appl. Mech. Mater.* **70** 28–32
[25] Irani K 2001 Theory and construction of blackbody calibration sources *Proc. SPIE* **4360** 347–62
[26] Quinn T J 1967 The calculation of the emissivity of cylindrical cavities giving near black-body radiation *Br. J. Appl. Phys.* **18** 1105–13
[27] Dulieu-Barton J M and Stanley P 1998 Development and applications of thermoelastic stress analysis *J. Strain Anal.* **33** 93–104
[28] Fruehmann R K, Dulieu-Barton J M and Quinn S 2008 On the thermoelastic response of woven composite materials *J. Strain Anal.* **43** 435–50